Spin-orbit coupling and linear crossings of dipolar magnons in van der Waals antiferromagnets

Liu, Jie; Wang, Lin; Shen, Ka

Important note
To cite this publication, please use the final published version (if applicable).
Please check the document version above.

Spin-orbit coupling and linear crossings of dipolar magnons in van der Waals antiferromagnets

Jie Liu [1,*] Lin Wang [2,*] and Ka Shen [1,†]

[1]*The Center for Advanced Quantum Studies and Department of Physics, Beijing Normal University, Beijing 100875, China*
[2]*Kavli Institute of Nanoscience, Delft University of Technology, P.O. Box 4056, 2600 GA Delft, The Netherlands*

A magnon spin-orbit coupling, induced by the dipole-dipole interaction, is derived in monoclinic-stacked bilayer honeycomb spin lattice with perpendicular magnetic anisotropy and antiferromagnetic interlayer coupling. Linear crossings are predicted in the magnon spectrum around the band minimum in Γ valley, as well as in the high-frequency range around the zone boundary. The linear crossings in K and K' valleys, which connect the acoustic and optical bands, can be gapped when the intralayer dipole-dipole or Kitaev interactions exceed the interlayer dipole-dipole interaction, resulting in a phase transition from semimetal to insulator. Our results are useful for analyzing the magnon spin dynamics and transport properties in van der Waals antiferromagnets.

I. INTRODUCTION

Since the experimental demonstrations of magnetism in two-dimensional (2D) van der Waals materials [1,2], 2D magnetic materials and the spin excitations therein have attracted great research interest. For CrI$_3$, one of the most important 2D magnetic materials, the strong atomic magnetic anisotropy makes it beyond the Heisenberg model addressed in the Mermin-Wagner theorem [3] and is responsible for the existence of the long-range magnetic order. Interestingly, the magnetic ground state of a bilayer CrI$_3$ is predicted to be either ferromagnetic or antiferromagnetic, depending on the way of stacking [4,5]. In particular, the monoclinic-stacked structure, as illustrated in Fig. 1(a), has been demonstrated experimentally to be a $\mathcal{PT}$-symmetric antiferromagnet, where the two ferromagnetic monolayers align antiferromagnetically with a relative shift along the zigzag direction [6].

The dynamics and transport properties of magnons, quanta of collective spin waves, have recently received intensive investigations in traditional bulk antiferromagnets [7–11]. One outstanding property of the magnons in antiferromagnets is the coexistence of different spin-polarized modes, which supplies more interesting physics due to the additional spin degrees of freedom [12,13], compared to magnons in ferromagnets. The studies in van der Waals antiferromagnets in this direction, however, remain limited. In bilayer CrI$_3$, for instance, the magnetization dynamics of the uniform mode has been observed only very recently through an ultrafast optical pump/magneto-optical Kerr probe technique [14] and magneto-Raman spectroscopy [15]. There is, so far, rare reporting on spin dynamics and transport of the propagating magnons.

In this paper, we perform a theoretical study on the magnon spectrum of the monoclinic-stacked antiferromagnetic bilayer

in Fig. 1(a) by taking into account the magnetic anisotropy, exchange interaction, and dipole-dipole interaction (DDI). Two linear crossings, as shown in Fig. 1(c), are predicted around the band minimum near the Γ point. Other linear crossing points in the short wavelength regime with THz frequency, e.g., those in K and K' valleys shown Figs. 1(f) and 1(g) and discussed in detail below, are also found. The effective Hamiltonian, which captures the main features, is derived. Moreover, a phase transition between semimetal and insulator will also be discussed.

II. MODEL AND HAMILTONIAN

We model our spin system by a Hamiltonian including magnetic anisotropy, Zeeman term, exchange interaction, and DDI:

$$H = \frac{K}{2} \sum_i \left(S_i^z\right)^2 + g\mu_B \sum_i \boldsymbol{S}_i \cdot \boldsymbol{B} - \sum_{\langle i,j \rangle} J_{ij} \boldsymbol{S}_i \cdot \boldsymbol{S}_j$$
$$+ \frac{\mu_0 (g\mu_B)^2}{2} \sum_{i \neq j} \frac{R_{ij}^2 (\boldsymbol{S}_i \cdot \boldsymbol{S}_j) - 3(\boldsymbol{R}_{ij} \cdot \boldsymbol{S}_i)(\boldsymbol{R}_{ij} \cdot \boldsymbol{S}_j)}{R_{ij}^5}.$$

(1)

For the stable classical antiferromagnetic ground state indicated in Fig. 1(a), we take the anisotropy parameter $K < 0$ and the nearest intralayer and interlayer exchange parameters $J > 0$ and $J' < 0$, respectively. The magnetic field is normal to the plane.

By applying the Holstein-Primakoff transformation [16],

$$S_a^z = S - a^\dagger a, \quad S_a^+ = \sqrt{2S - a^\dagger a}\, a,$$
$$S_d^z = -S + d^\dagger d, \quad S_d^+ = d^\dagger \sqrt{2S - d^\dagger d},$$

(2)

we derive the magnon Hamiltonian under the basis $(a_{1k}, a_{2k}, d_{1k}, d_{2k}, a_{1-k}^\dagger, a_{2-k}^\dagger, d_{1-k}^\dagger, d_{2-k}^\dagger)^T$ with a_{ik} (d_{ik}) and $a_{ik}^\dagger$ $(d_{ik}^\dagger)$ representing the magnon annihilation and creation operators for the ith sublattice in the top (bottom) layer,

———————
*These authors contributed equally to this paper.
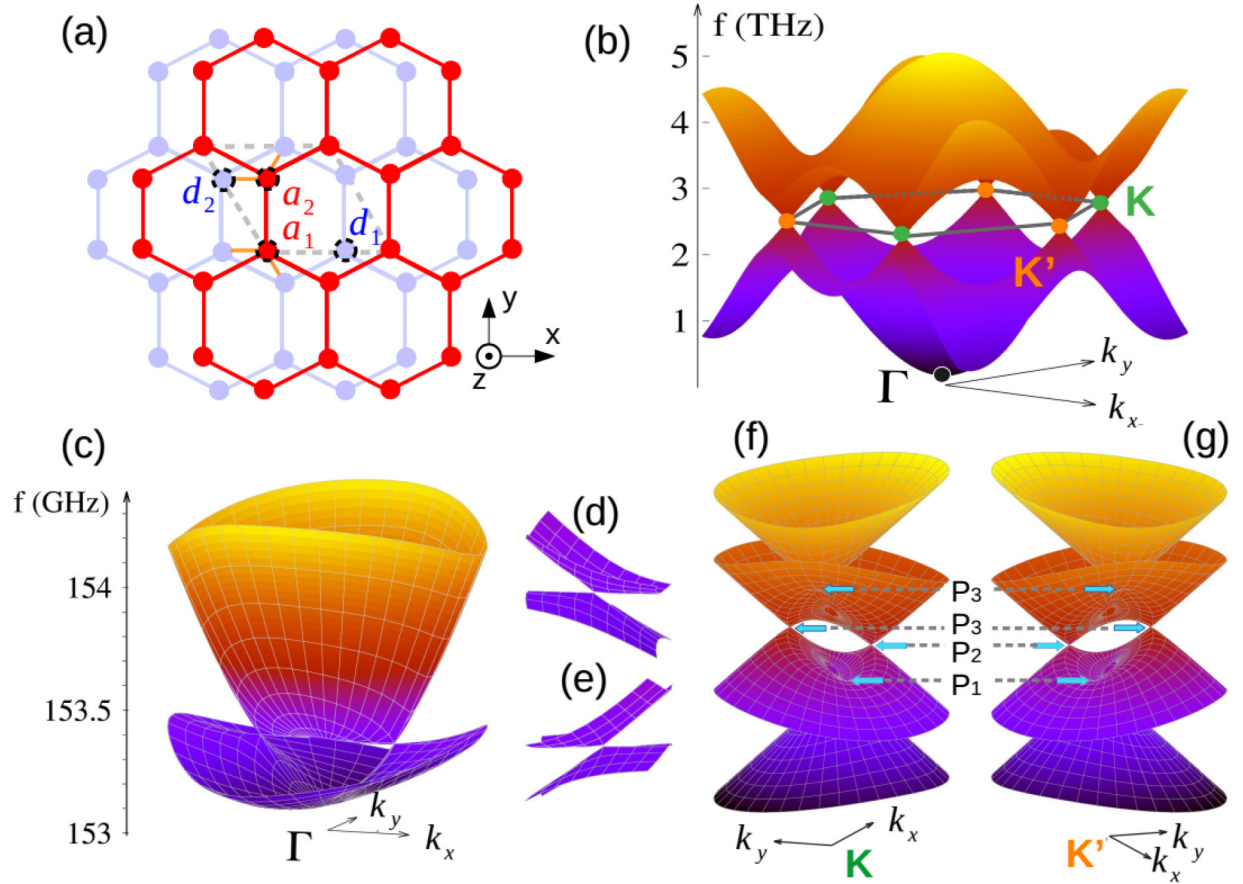†kashen@bnu.edu.cn

FIG. 1. (a) The monoclinic lattice of bilayer CrI$_3$ with antiferromagnetic interlayer coupling. Only the magnetic atoms are shown. The coordinates of atoms within the unit cell are $\mathbf{r}_{a_1} = (0, 0, \eta_z)a_0$, $\mathbf{r}_{a_2} = (0, 1, \eta_z)a_0$, $\mathbf{r}_{d_1} = (2\sqrt{3}/3, 0, -\eta_z)a_0$, and $\mathbf{r}_{d_2} = (-\sqrt{3}/3, 1, -\eta_z)a_0$ with a_0 being the shortest distance between neighboring atoms. The interlayer distance is $2\eta_z a_0$. The ground-spin configuration corresponds to the spins in the upper (lower) layer colored in red (blue), orientating along $\hat{z}$ ($-\hat{z}$) direction. The orange bonds stand for those bearing antiferromagnetic interlayer coupling. (b) Full magnon spectrum and the fine structures in (c) Γ, (f) K, and (g) K' valleys. (d) and (e) are the enlarged view around the left and right crossing points, respectively, in Γ valley.

respectively. The first line of Hamiltonian Eq. (1) leads to [13,17]

$$
H^0_{\mathbf{k},-\mathbf{k}} = \begin{pmatrix} [H_a^{ij}] & 0 & 0 & [\lambda_{\mathbf{k}}^{ij}] \\ 0 & [H_d^{ij}] & [\lambda_{\mathbf{k}}^{ij}]^{\dagger} & 0 \\ 0 & [\lambda_{\mathbf{k}}^{ij}] & [H_a^{ij}] & 0 \\ [\lambda_{\mathbf{k}}^{ij}]^{\dagger} & 0 & 0 & [H_d^{ij}] \end{pmatrix}, \quad (3)
$$

where each block is a 2×2 matrix with $i, j = 1, 2$ and the diagonal ones read

$$
[H_{a(d)}^{ij}] = \begin{pmatrix} \epsilon_{a(d)} & \lambda_{\mathbf{k}} \\ \lambda_{\mathbf{k}}^* & \epsilon_{a(d)} \end{pmatrix}. \quad (4)
$$

The matrix elements are defined as

$$
\epsilon_a = \omega_{\text{ex}} + 2\omega'_{\text{ex}} + \omega_{\text{an}} - \omega_H, \quad (5)
$$

$$
\epsilon_d = \omega_{\text{ex}} + 2\omega'_{\text{ex}} + \omega_{\text{an}} + \omega_H, \quad (6)
$$

$$
\lambda_{\mathbf{k}} = -\omega_{\text{ex}}\gamma_{\mathbf{k}}, \quad (7)
$$

$$
\lambda_{\mathbf{k}}^{ij} = \omega'_{\text{ex}}\gamma_{\mathbf{k}}^{ij}, \quad (8)
$$

with $\omega_{\text{ex}} = 3SJ$, $\omega_{\text{an}} = -KS$, $\omega'_{\text{ex}} = -SJ'$, and $\omega_H = g\mu_B B$. The form factors are $\gamma_{\mathbf{k}} = \frac{1}{3}\sum_{i=1}^3 e^{i\mathbf{k}\cdot\boldsymbol{\delta}_i}$ and $\gamma_{\mathbf{k}}^{ij} = e^{i\mathbf{k}\cdot\boldsymbol{\delta}'_{ij}}$ with the relative coordinates between the neighboring atoms being

$$
\boldsymbol{\delta}_1 = (0, a_0, 0), \quad (9)
$$

$$
\boldsymbol{\delta}_2 = \left(\frac{\sqrt{3}a_0}{2}, -\frac{a_0}{2}, 0\right), \quad (10)
$$

$$
\boldsymbol{\delta}_3 = \left(-\frac{\sqrt{3}a_0}{2}, -\frac{a_0}{2}, 0\right), \quad (11)
$$

$$
\boldsymbol{\delta}'_{11} = \boldsymbol{\delta}'_{22} = \left(-\frac{\sqrt{3}a_0}{3}, 0, -2\eta_z a_0\right), \quad (12)
$$

$$
\boldsymbol{\delta}'_{12} = \left(-\frac{\sqrt{3}a_0}{6}, \frac{a_0}{2}, -2\eta_z a_0\right), \quad (13)
$$

$$
\boldsymbol{\delta}'_{21} = \left(\frac{\sqrt{3}a_0}{6}, \frac{a_0}{2}, -2\eta_z a_0\right). \quad (14)
$$

The DDI term, i.e., the second line in Hamiltonian Eq. (1), gives

$$H_{\boldsymbol{k},-\boldsymbol{k}}^{\mathrm{DDI}} = \begin{pmatrix} [A_{\boldsymbol{k}}^{a_i a_j}] & [B_{\boldsymbol{k}}^{d_i a_j}]^{\dagger} & [B_{\boldsymbol{k}}^{a_i a_j}]^{\dagger} & [A_{\boldsymbol{k}}^{d_i a_j}]^{\dagger} \\ [B_{\boldsymbol{k}}^{d_i a_j}] & [A_{\boldsymbol{k}}^{d_i d_j}] & [A_{\boldsymbol{k}}^{d_i a_j}] & [B_{\boldsymbol{k}}^{d_i d_j}] \\ [B_{\boldsymbol{k}}^{a_i a_j}] & [A_{\boldsymbol{k}}^{d_i a_j}]^{\dagger} & [A_{\boldsymbol{k}}^{a_i a_j}] & [B_{\boldsymbol{k}}^{a_i d_j}] \\ [A_{\boldsymbol{k}}^{d_i a_j}] & [B_{\boldsymbol{k}}^{d_i d_j}]^{\dagger} & [B_{\boldsymbol{k}}^{a_i d_j}]^{\dagger} & [A_{\boldsymbol{k}}^{d_i d_j}] \end{pmatrix}. \quad (15)$$

The matrix elements are defined as

$$A_{\boldsymbol{k}}^{\alpha\beta} = -\frac{S\mu_0(g\mu_B)^2}{2}G_{\boldsymbol{k}}^{\alpha\beta}, \quad (16)$$

$$B_{\boldsymbol{k}}^{\alpha\beta} = \frac{S\mu_0(g\mu_B)^2}{2}F_{\boldsymbol{k}}^{\alpha\beta}, \quad (17)$$

in which

$$F_{\boldsymbol{k}}^{\alpha\beta} = -3\sum_{mn}\frac{(X_{mn}^{\alpha\beta} - iY_{mn}^{\alpha\beta})^2}{(R_{mn}^{\alpha\beta})^5}e^{i\boldsymbol{k}\cdot\boldsymbol{R}_{mn}^{\alpha\beta}}, \quad (18)$$

$$G_{\boldsymbol{k}}^{\alpha\beta} = \sum_{mn}\frac{(R_{mn}^{\alpha\beta})^2 - 3(Z_{mn}^{\alpha\beta})^2}{(R_{mn}^{\alpha\beta})^5}e^{i\boldsymbol{k}\cdot\boldsymbol{R}_{mn}^{\alpha\beta}}. \quad (19)$$

with $\boldsymbol{R}_{mn}^{\alpha\beta} = m\boldsymbol{v}_1 + n\boldsymbol{v}_2 + \boldsymbol{r}_\beta - \boldsymbol{r}_\alpha$. The unit translation vectors read

$$\boldsymbol{v}_1 = (\sqrt{3}a_0, 0, 0), \quad (20)$$

$$\boldsymbol{v}_2 = \left(-\frac{\sqrt{3}}{2}a_0, \frac{3}{2}a_0, 0\right). \quad (21)$$

The entire magnon spectrum thus can be calculated from Hamiltonian Eqs. (3) and (15). The main features in the absence of the magnetic field are plotted in Fig. 1, for which we have adopted the parameters in bilayer CrI$_3$ with $S = 3/2$, $K = -0.49$ meV, $J = 2.2$ meV, $J' = -0.04$ meV, $a_0 = 3.98$ Å, and $2\eta_z a_0 = 3.98$ Å [4,18].

III. MAGNON SPIN-ORBIT COUPLING

For a better understanding of the numerical results, we perform an analytical analysis, for which we ignore the particle-hole coupling, i.e., the 4×4 off-diagonal blocks in Hamiltonian Eqs. (3) and (15), by considering the fact that the interlayer exchange interaction ($\omega_{\mathrm{ex}}' \sim 0.06$ meV) and the DDI ($|A(B)_{\boldsymbol{k}}^{\alpha\beta}| \sim 0.01$ meV) in bilayer CrI$_3$ are much weaker than the particle-hole splitting (twice of the magnon gap) due to the anisotropy ($\omega_{\mathrm{an}} \sim 0.7$ meV) and intralayer exchange interaction ($\omega_{\mathrm{ex}} \sim 10$ meV), and therefore do not cause a qualitative change in the magnon spectrum (unless otherwise clarified in Sec. III C). Then we can restrict our discussion within the particle subspace $(a_{1\boldsymbol{k}}, a_{2\boldsymbol{k}}, d_{1\boldsymbol{k}}, d_{2\boldsymbol{k}})^T$. The reduced Hamiltonian can be in general written as

$$H_{\boldsymbol{k}} = \begin{pmatrix} \epsilon_a + \epsilon_{\boldsymbol{k}}' & \lambda_{\boldsymbol{k}} + \lambda_{\boldsymbol{k}}' & \zeta_{\boldsymbol{k}}^* & \eta_{\boldsymbol{k}}^* \\ \lambda_{\boldsymbol{k}}^* + \lambda_{\boldsymbol{k}}'^* & \epsilon_a + \epsilon_{\boldsymbol{k}}' & \eta_{\boldsymbol{k}}'^* & \zeta_{\boldsymbol{k}}^* \\ \zeta_{\boldsymbol{k}} & \eta_{\boldsymbol{k}}' & \epsilon_d + \epsilon_{\boldsymbol{k}}' & \lambda_{\boldsymbol{k}} + \lambda_{\boldsymbol{k}}' \\ \eta_{\boldsymbol{k}} & \zeta_{\boldsymbol{k}} & \lambda_{\boldsymbol{k}}^* + \lambda_{\boldsymbol{k}}'^* & \epsilon_d + \epsilon_{\boldsymbol{k}}' \end{pmatrix}, \quad (22)$$

with intralayer DDI parameters

$$\epsilon_{\boldsymbol{k}}' = A_{\boldsymbol{k}}^{a_1 a_1} = A_{\boldsymbol{k}}^{d_1 d_1}, \quad (23)$$

$$\lambda_{\boldsymbol{k}}' = A_{\boldsymbol{k}}^{a_1 a_2} = A_{\boldsymbol{k}}^{d_1 d_2}, \quad (24)$$

and interlayer ones

$$\zeta_{\boldsymbol{k}} = B_{\boldsymbol{k}}^{d_1 a_1}, \quad (25)$$

$$\eta_{\boldsymbol{k}} = B_{\boldsymbol{k}}^{d_2 a_1}, \quad (26)$$

$$\eta_{\boldsymbol{k}}' = B_{\boldsymbol{k}}^{d_1 a_2}. \quad (27)$$

It is convenient to transform Hamiltonian Eq. (22) into the representation under the basis of the eigenstates of intralayer interaction, i.e., $(a_{\boldsymbol{k}}^+, d_{\boldsymbol{k}}^+, a_{\boldsymbol{k}}^-, d_{\boldsymbol{k}}^-)$ with

$$a(d)_{\boldsymbol{k}}^{\pm} = \frac{1}{\sqrt{2}}\left[a(d)_{1\boldsymbol{k}} \pm \frac{\lambda_{\boldsymbol{k}}^* + \lambda_{\boldsymbol{k}}'^*}{|\lambda_{\boldsymbol{k}} + \lambda_{\boldsymbol{k}}'|}a(d)_{2\boldsymbol{k}}\right]. \quad (28)$$

The Hamiltonian Eq. (22) thus becomes

$$\tilde{H}_{\boldsymbol{k}} = \begin{pmatrix} \epsilon_{a,\boldsymbol{k}}^+ & \zeta_{\boldsymbol{k}}^* + \eta_{+,\boldsymbol{k}}^* & 0 & \eta_{-,\boldsymbol{k}}^* \\ \zeta_{\boldsymbol{k}} + \eta_{+,\boldsymbol{k}} & \epsilon_{d,\boldsymbol{k}}^+ & -\eta_{-,\boldsymbol{k}} & 0 \\ 0 & -\eta_{-,\boldsymbol{k}}^* & \epsilon_{a,\boldsymbol{k}}^- & \zeta_{\boldsymbol{k}}^* - \eta_{+,\boldsymbol{k}}^* \\ \eta_{-,\boldsymbol{k}} & 0 & \zeta_{\boldsymbol{k}} - \eta_{+,\boldsymbol{k}} & \epsilon_{d,\boldsymbol{k}}^- \end{pmatrix}, \quad (29)$$

with

$$\epsilon_{a(d),\boldsymbol{k}}^{\pm} = \epsilon_{a(d)} + \epsilon_{\boldsymbol{k}}' \pm |\lambda_{\boldsymbol{k}} + \lambda_{\boldsymbol{k}}'|, \quad (30)$$

$$\eta_{\pm,\boldsymbol{k}} = \frac{(\lambda_{\boldsymbol{k}}^* + \lambda_{\boldsymbol{k}}'^*)\eta_{\boldsymbol{k}}' \pm (\lambda_{\boldsymbol{k}} + \lambda_{\boldsymbol{k}}')\eta_{\boldsymbol{k}}}{2|\lambda_{\boldsymbol{k}} + \lambda_{\boldsymbol{k}}'|}. \quad (31)$$

Here, the superscripts $-$ and $+$ denote the acoustic and optical bands, respectively. Since the excitations, $a_{\boldsymbol{k}}$ and $d_{\boldsymbol{k}}$, have opposite spin polarization [13], Hamiltonian Eq. (29) reveals that the interlayer DDI introduces not only an intraband spin-orbit coupling to the acoustic and optical branches separately via $\zeta_{\boldsymbol{k}} - \eta_{+,\boldsymbol{k}}$ and $\zeta_{\boldsymbol{k}} + \eta_{+,\boldsymbol{k}}$, but also an interband spin-orbit coupling scaled by $\eta_{-,\boldsymbol{k}}$. The momentum dependence of these spin-orbit parameters are plotted in Fig. 2, in which inactive momentum points with vanishing value are observed. The situation of the acoustic branch, i.e., $\zeta_{\boldsymbol{k}} - \eta_{+,\boldsymbol{k}}$, is explicitly shown in Fig. 3. The vanishing value around the Γ point and the boundary of Brillouin zone explains the formation of nodal points shown in Fig. 1(c). The orientation of the spin-orbit field, as indicated by the colored arrows, varies with wave vector around the nodal points.

A. Effective Hamiltonian and nodal points in Γ valley

In the vicinity of the Γ-point, $\lambda_{\boldsymbol{k}} \simeq -(1 - k^2 a_0^2/4)\omega_{\mathrm{ex}}$. The acoustic modes and the optical modes are well separated in frequency. Thanks to the relation $|\eta_{-,\boldsymbol{k}}| \ll \omega_{\mathrm{ex}}$, one can treat them separately. The Hamiltonian thus reduces to two subsystems involving only the spin degree of freedom

$$\tilde{H}_{\boldsymbol{k}}^{\pm} = \begin{pmatrix} \epsilon_{a,\boldsymbol{k}}^{\pm} & \zeta_{\boldsymbol{k}}^* \pm \eta_{+,\boldsymbol{k}}^* \\ \zeta_{\boldsymbol{k}} \pm \eta_{+,\boldsymbol{k}} & \epsilon_{d,\boldsymbol{k}}^{\pm} \end{pmatrix}, \quad (32)$$
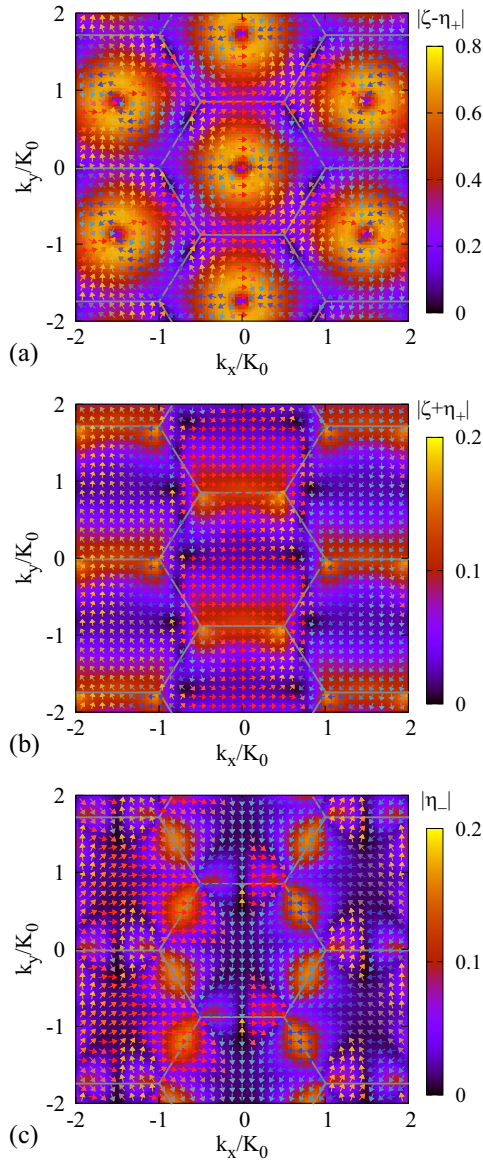
FIG. 2. DDI-induced intraband spin-orbit parameters of (a) acoustic and (b) optical magnon bands and (c) the interband coupling. The arrows stand for the arguments of these complex parameters. $K_0 = 4\pi/(3\sqrt{3}a_0)$.

where the diagonal and off-diagonal components read

$$\epsilon_{a(d),\boldsymbol{k}}^{\pm} = \epsilon_{a(d)} - \frac{S\mu_0(g\mu_B)^2}{2}\left(G_{\boldsymbol{k}}^{a_1a_1} \pm G_{\boldsymbol{k}}^{a_1a_2}\right)$$
$$\pm \left(1 - \frac{a_0^2}{4}k^2\right)\omega_{\mathrm{ex}}, \tag{33}$$

$$\zeta_{\boldsymbol{k}} \pm \eta_{+,\boldsymbol{k}} = \frac{S\mu_0(g\mu_B)^2}{2}\left(F_{\boldsymbol{k}}^{d_1a_1} \mp \frac{F_{\boldsymbol{k}}^{d_1a_2} + F_{\boldsymbol{k}}^{d_2a_1}}{2}\right). \tag{34}$$

After evaluating the summation in $F_{\boldsymbol{k}}^{\alpha\beta}$ and $G_{\boldsymbol{k}}^{\alpha\beta}$ in the long wavelength limit, as explained in Appendix A, we achieve an analytical expression:

$$\tilde{H}_{\boldsymbol{k}}^{\pm} = \bar{\epsilon}_{\boldsymbol{k}}^{\pm} + (\omega_H\hat{z} + \boldsymbol{\Delta}_{\boldsymbol{k}}^{\pm})\cdot\boldsymbol{\sigma}. \tag{35}$$
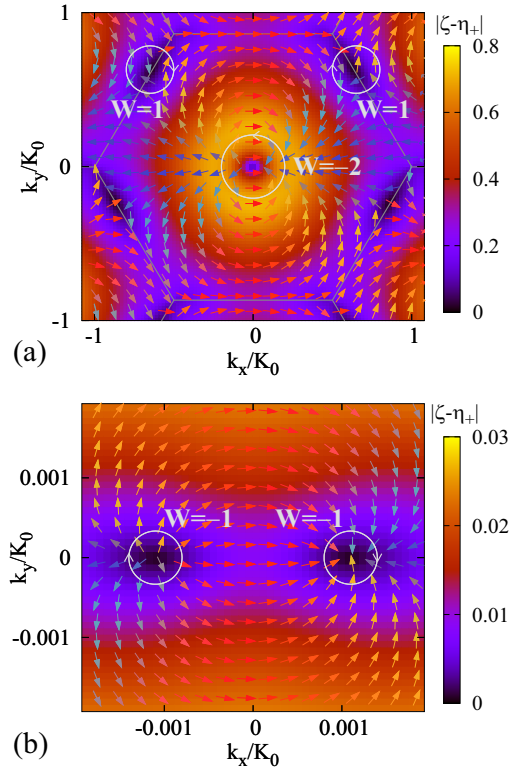

FIG. 3. DDI-induced intraband spin-orbit field of the acoustic magnon bands (a) in first Brillouin zone and (b) in the vicinity of Γ point. W is the winding number of each loop.

Here, the spin-independent energy can be expressed as

$$\bar{\epsilon}_{\boldsymbol{k}}^{-} = \omega_{\mathrm{an}} + 2\omega_{\mathrm{ex}}' + f_z + f_z' + v_0 k + \omega_{\mathrm{ex}}\frac{a_0^2}{4}k^2, \tag{36}$$

$$\bar{\epsilon}_{\boldsymbol{k}}^{+} = \omega_{\mathrm{an}} + 2(\omega_{\mathrm{ex}} + \omega_{\mathrm{ex}}') + f_z - f_z' - \omega_{\mathrm{ex}}\frac{a_0^2}{4}k^2, \tag{37}$$

and the spin-orbit fields are

$$\boldsymbol{\Delta}_{\boldsymbol{k}}^{-} = (v_0 k\cos 2\phi_{\boldsymbol{k}} - f_0, v_0 k\sin 2\phi_{\boldsymbol{k}}, 0), \tag{38}$$

$$\boldsymbol{\Delta}_{\boldsymbol{k}}^{+} = (-3f_0, 0, 0), \tag{39}$$

where f_0 and v_0 are positive real numbers. It is interesting to note that while the spin-orbit coupling of the optical band is a simple constant, the one of the acoustic band contains an additional contribution varying with the direction of momentum. Such an angular dependence is a common feature of dipolar field in the long wavelength limit [13]. Another important feature one can observe from spin-orbit field Eq. (38) is that, distinct from the three-dimensional (3D) case [13], the magnitude of the angular dependent term here is linear in k.

Apparently, the spin-orbit field Eq. (38) vanishes at $\boldsymbol{k}_{\pm} = (\pm f_0/v_0, 0) \simeq (\pm 0.001 K_0, 0)$, which well explains the numerical results in Fig. 3(b). At $\omega_H = 0$, $\boldsymbol{k}_{\pm}$ corresponds to the two nodal points in Fig. 1(c). We expand the spin-orbit coupling Eq. (38) near $\boldsymbol{k} = \boldsymbol{k}_{\pm} + \tilde{\boldsymbol{k}}$ and obtain an effective

Hamiltonian up to the linear order in $\tilde{\boldsymbol{k}}$,

$$H_{\pm}^{-}(\tilde{\boldsymbol{k}}) = \pm(v_0 \tilde{k}_x \sigma_x + 2v_0 \tilde{k}_y \sigma_y)$$

$$= \begin{pmatrix} 0 & \pm v_0(\tilde{k}_x - 2i\tilde{k}_y) \\ \pm v_0(\tilde{k}_x + 2i\tilde{k}_y) & 0 \end{pmatrix}, \quad (40)$$

where the spin-independent term $\bar{\epsilon}_{\boldsymbol{k}_{\pm}}^{-}$ has been discarded. This Hamiltonian has chiral symmetry $CH_{\pm}^{-}(\tilde{\boldsymbol{k}})C^{-1} = -H_{\pm}^{-}(\tilde{\boldsymbol{k}})$ with $C = \sigma_z$. As a result, the chirality of the nodal points is characterized by the winding number,

$$W = (1/2\pi i) \oint_{\mathrm{L}} d\xi(\tilde{\boldsymbol{k}})/\xi(\tilde{\boldsymbol{k}}), \quad (41)$$

where the integration performed over a closed loop around the nodal point and $\xi_{\pm}(\tilde{\boldsymbol{k}})$ is defined as the phase factor of the off-diagonal matrix element in Eq. (40), i.e.,

$$\xi_{\pm}(\tilde{\boldsymbol{k}}) = \pm \frac{\tilde{k}_x - 2i\tilde{k}_y}{|\tilde{k}_x - 2i\tilde{k}_y|}. \quad (42)$$

This leads to chirality of -1 for both nodal points. The nonzero chirality, the linear crossing, and the twofold degeneracy together indicate that these nodal points can be regarded as a magnon analog of the 2D Weyl points recently proposed in an electronic system [19].

As shown in Fig. 3(b), the winding number -1 also coincides with the direct observation of a 2π rotation of the spin-orbit field through a closed loop around each nodal point. The total winding number of the Γ valley [for a single loop besieging both nodal points in Fig. 3(a)] is therefore -2, being the same as the one around the dipolar-induced nodal line in 3D cubic lattice [20]. Figure 3(a) shows that another two nodal points at the zone boundary both have winding number $+1$, compensating the chirality from $\boldsymbol{k}_{\pm}$ near Γ valley. In contrast to the 3D Weyl points, which are robust against any perturbation [21–24], the 2D Weyl points can be gapped by particular perturbation [19]. In the present case, for example, the inclusion of a nonvanishing ω_H due to an out-of-plane magnetic field, according to the effective Hamiltonian Eq. (35), opens a gap at the crossing points, very similar to the situation in 2D electron gas with Dresselhaus- or Rashba-type in-plane spin-orbit field.

B. Nodal points in K and K' valley

At K and K' points, the band splitting $|\lambda_{\boldsymbol{k}} + \lambda'_{\boldsymbol{k}}|$ vanishes, therefore, one has to treat the acoustic and optical bands together by using the complete 4×4 Hamiltonian Eq. (29). By expanding the Hamiltonian around these points,

$$\boldsymbol{k} = \boldsymbol{K}(\boldsymbol{K}') + q(\cos\theta_q, \sin\theta_q), \quad (43)$$

with $\boldsymbol{K}(\boldsymbol{K}') = (\mp K_0, 0)$ and $q \ll K_0$, we obtain

$$\eta_{\pm,K+q} \simeq -\zeta_K[e^{-i\theta_q} \pm e^{i(\theta_q - 2\pi/3)}]/2, \quad (44)$$

$$\eta_{\pm,K'+q} \simeq \pm\zeta_{K'}[e^{-i\theta_q} \pm e^{i(\theta_q + 2\pi/3)}]/2, \quad (45)$$

with $\zeta_{K'} = \zeta_K^*$. The derivation of Eqs. (44) and (45) is given in Appendix B. At $\theta_q = \pm\pi/3$, all elements of the off-diagonal blocks depending solely on $\eta_{-,\boldsymbol{k}}$ vanish for K and K' valleys, respectively. The four dispersion curves along this momentum line become linear in q, i.e., $\bar{\epsilon}_K - v_F q \pm \sqrt{3}|\zeta_K|$ and

$\bar{\epsilon}_K + v_F q \pm |\zeta_K|$. The intersections between them give rise to four nodal points in each valley, namely,

$$\boldsymbol{k}_{1,\tau} = \frac{(\sqrt{3}+1)|\zeta_K|}{2v_F}\left(\frac{\tau}{2}, \frac{\sqrt{3}}{2}\right), \quad (46)$$

$$\boldsymbol{k}_{2,\tau} = \frac{(\sqrt{3}-1)|\zeta_K|}{2v_F}\left(\frac{\tau}{2}, \frac{\sqrt{3}}{2}\right), \quad (47)$$

$$\boldsymbol{k}_{3,\tau} = \frac{(\sqrt{3}+1)|\zeta_K|}{2v_F}\left(-\frac{\tau}{2}, -\frac{\sqrt{3}}{2}\right), \quad (48)$$

$$\boldsymbol{k}_{4,\tau} = \frac{(\sqrt{3}-1)|\zeta_K|}{2v_F}\left(-\frac{\tau}{2}, -\frac{\sqrt{3}}{2}\right). \quad (49)$$

Here, τ is the valley index with K ($\tau = 1$) and K' ($\tau = -1$). This is consistent with the spectrum from a full calculation plotted in Figs. 1(f) and 1(g). To uncover the nature of these nodal points, we again expand the Hamiltonian near $\boldsymbol{k} = \boldsymbol{k}_{i,\tau} + \tilde{\boldsymbol{k}}$ and derive a 2×2 effective Hamiltonian for each nodal point under the basis of the two branches involving

$$H_{1,\tau} = n_{z,\tau}s_z - n_{\parallel,\tau}(\tau s_x + s_y), \quad (50)$$

$$H_{2,\tau} = n_{z,\tau}s_z + n_{\parallel,\tau}(\tau s_x - s_y), \quad (51)$$

$$H_{3,\tau} = -n_{z,\tau}s_z - n_{\parallel,\tau}(\tau s_x - s_y), \quad (52)$$

$$H_{4,\tau} = -n_{z,\tau}s_z + n_{\parallel,\tau}(\tau s_x + s_y), \quad (53)$$

where

$$n_{z,\tau} = (v_F/2)(\tilde{k}_x\tau + \sqrt{3}\tilde{k}_y), \quad (54)$$

$$n_{\parallel,\tau} = (v_F/4)(\sqrt{3}\tilde{k}_x\tau - \tilde{k}_y). \quad (55)$$

Here, $s_{i=x,y,z}$ are Pauli matrices. These effective Hamiltonians can be classified into two groups, i.e.,

$$H_{\pm} = n_z s_z + n_{\parallel}(s_x \pm s_y), \quad (56)$$

which have chiral symmetry

$$C_{\pm} = (s_x \mp s_y)/\sqrt{2}, \quad (57)$$

and therefore can be brought to a block off-diagonal form by a unitary transformation $U_{\pm}$.

$$U_{\pm}^{-1}H_{\pm}U_{\pm} = \begin{pmatrix} 0 & -n_z \mp i\sqrt{2}n_{\parallel} \\ -n_z \pm i\sqrt{2}n_{\parallel} & 0 \end{pmatrix}, \quad (58)$$

with

$$U_{\pm} = \frac{1}{2}\begin{pmatrix} 1 \pm i & -1 \mp i \\ \sqrt{2} & \sqrt{2} \end{pmatrix}. \quad (59)$$

By substituting the phase factor of the off-diagonal matrix element in Hamiltonian Eq. (58), i.e.,

$$\xi_{\pm} = -\frac{n_z \pm i\sqrt{2}n_{\parallel}}{|n_z \pm i\sqrt{2}n_{\parallel}|} \quad (60)$$

into Eq. (41), we find that all four nodal points near K (K') valley have the same chirality of $+1$ (-1). By considering their twofold degeneracy and the linear dispersion nearby, we conclude that these nodal points are also 2D Weyl points [19].
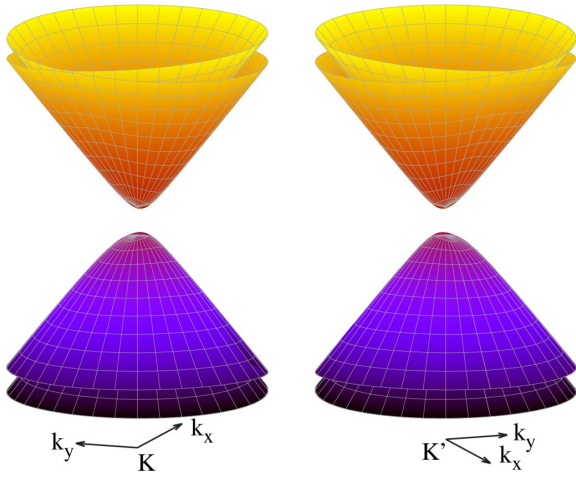
FIG. 4. Magnon spectrum around the K and K' points from the calculation, in which the interlayer DDI is suppressed by increasing the interlayer distance by 30%.

C. Phase transition from semimetal and insulator

We should point out that the particle-hole coupling due to the intralayer DDI, which has been neglected in the above analysis, actually is able to cause quantitative or even qualitative changes for different parameter choices. Specifically, the nodal points $P_{1\text{-}4}$ in Figs. 1(f) and 1(g) from full calculation are found to deviate from the momentum line with $\theta_q = \pm \pi/3$. By increasing the ratio between the strengths of the intra- and interlayer DDI via decreasing the interlayer distance, P_2 and P_3 become closer and finally overlap at a critical ratio. When this ratio increases further, a global gap is opened between the acoustic and optical branches, leading to a transition from semimetal phase to insulating phase. The fine structure around K and K' points for the gapped phase is plotted in Fig. 4, for which the interlayer distance in enhanced by 30%.

According to Eq. (B21), the particle-hole coupling induced by intralayer DDI gives

$$B_{\boldsymbol{K}(\boldsymbol{K}')}^{a_1 a_2} = B_{\boldsymbol{K}'(\boldsymbol{K})}^{a_2 a_1} = f_K [1 + e^{i\frac{2\pi}{3}(1\pm 1)} + e^{-i\frac{2\pi}{3}(1\pm 1)}], \quad (61)$$

which suggests $B_{\boldsymbol{K}}^{a_1 a_2} = B_{\boldsymbol{K}'}^{a_2 a_1} = 0$ and $B_{\boldsymbol{K}}^{a_2 a_1} = B_{\boldsymbol{K}'}^{a_1 a_2} \neq 0$. Similarly, one has $B_{\boldsymbol{K}}^{d_1 d_2} = B_{\boldsymbol{K}'}^{d_2 d_1} = 0$ and $B_{\boldsymbol{K}}^{d_2 d_1} = B_{\boldsymbol{K}'}^{d_1 d_2} \neq 0$.

On the other hand, as recently shown in Ref. [25], the Kitaev interaction, an anisotropic term of the intralayer exchange interaction between the nearest-neighboring Cr atoms, can produce a similar insulating phase in single layer CrI_3. To examine its role in our bilayer structure, we take into account this additional intralayer interaction [26,27],

$$H^{\mathrm{K}} = -K^A \sum_{\langle i,j \rangle} \left(\boldsymbol{S}_i \cdot \hat{\boldsymbol{p}}_{\boldsymbol{R}_{ij}} \right) \cdot \left(\boldsymbol{S}_j \cdot \hat{\boldsymbol{p}}_{\boldsymbol{R}_{ij}} \right), \quad (62)$$

where

$$\hat{\boldsymbol{p}}_{\delta_1} = \left(-\sqrt{\frac{2}{3}}, 0, \sqrt{\frac{1}{3}} \right), \quad (63)$$

$$\hat{\boldsymbol{p}}_{\delta_2} = \left(\sqrt{\frac{1}{6}}, \sqrt{\frac{1}{2}}, \sqrt{\frac{1}{3}} \right), \quad (64)$$

$$\hat{\boldsymbol{p}}_{\delta_3} = \left(\sqrt{\frac{1}{6}}, -\sqrt{\frac{1}{2}}, \sqrt{\frac{1}{3}} \right). \quad (65)$$

After applying the aforementioned standard procedures, we obtain

$$H^K = \begin{pmatrix} [H_{\boldsymbol{k}}^{'ij}] & 0 & [\mathcal{K}_{\boldsymbol{k}}^{ij}]^\dagger & 0 \\ 0 & [H_{\boldsymbol{k}}^{'ij}] & 0 & [\mathcal{K}_{\boldsymbol{k}}^{ij}] \\ [\mathcal{K}_{\boldsymbol{k}}^{ij}] & 0 & [H_{\boldsymbol{k}}^{'ij}] & 0 \\ 0 & [\mathcal{K}_{\boldsymbol{k}}^{ij}]^\dagger & 0 & [H_{\boldsymbol{k}}^{'ij}] \end{pmatrix}, \quad (66)$$

where the nonvanishing blocks are expressed as

$$[H_{\boldsymbol{k}}^{'ij}] = K^A S \begin{pmatrix} 1 & -\gamma_{\boldsymbol{k}} \\ -\gamma_{\boldsymbol{k}}^* & 1 \end{pmatrix}, \quad (67)$$

$$[\mathcal{K}_{\boldsymbol{k}}^{ij}] = K^A S \begin{pmatrix} 0 & -\tilde{\gamma}_{\boldsymbol{k}} \\ -\tilde{\gamma}_{-\boldsymbol{k}} & 0 \end{pmatrix}. \quad (68)$$

The form factor $\gamma_{\boldsymbol{k}}$ here is the same as above and

$$\tilde{\gamma}_{\boldsymbol{k}} = \frac{1}{3} (e^{i\boldsymbol{k} \cdot \boldsymbol{\delta}_1} + e^{i2\pi/3 + i\boldsymbol{k} \cdot \boldsymbol{\delta}_2} + e^{-i2\pi/3 + i\boldsymbol{k} \cdot \boldsymbol{\delta}_3}). \quad (69)$$

As one may notice, the diagonal blocks can be included into the Hamiltonian Eq. (4) by simply replacing the exchange parameter ω_{ex} by $\omega_{\mathrm{ex}} + K^A S$. The off-diagonal blocks are additive to those from intralayer DDI $[B_{\boldsymbol{k}}^{a_i a_j}]$ and $[B_{\boldsymbol{k}}^{d_i d_j}]$. In particular, at K and K' points, we have

$$\tilde{\gamma}_{K(K')} = \frac{1}{3} [1 + e^{i\frac{2\pi}{3}(1\mp 1)} + e^{-i\frac{2\pi}{3}(1\mp 1)}], \quad (70)$$

which contains the same factor as Eq. (61) and gives $\mathcal{K}_{\boldsymbol{K}}^{21} = \mathcal{K}_{\boldsymbol{K}'}^{12} = 0$ but $\mathcal{K}_{\boldsymbol{K}}^{12} = \mathcal{K}_{\boldsymbol{K}'}^{21} \neq 0$. This indicates that the Kitaev affects the spectrum of K and K' valleys in the same way as the intralayer DDI.

Therefore, a material with weaker Kitaev interaction is preferred for experimental observation of $K(K')$-valley nodal points. Another option would be to use an artificial structure to avoid anisotropic exchange interaction. Nevertheless, the linear crossings between the two spin bands in the Γ-valley are robust against the intralyer DDI and Kitaev interaction, even in the insulating phase.

D. Discussion on $\mathcal{PT}$ symmetry

Before closing this paper, we would like to discuss the role of the $\mathcal{PT}$ symmetry in magnonic systems. It is well known that in a $\mathcal{PT}$-symmetric fermionic system, Weyl fermions are forbidden because the $\mathcal{PT}$ symmetry introduces twofold degeneracy of Weyl cones [28]. In the present magnonic case, such a degeneracy is removed by the interlayer DDI, which can be understood as follows. Without any interlayer coupling, for any magnon mode in the top layer $a_{\boldsymbol{k}}$, one can find its $\mathcal{PT}$ partner in the bottom layer $b_{\boldsymbol{k}}$. The bosonic nature of magnons requires $(\mathcal{PT})^2 = 1$, and therefore $\mathcal{PT} a_{\boldsymbol{k}} = b_{\boldsymbol{k}}$ and $\mathcal{PT} b_{\boldsymbol{k}} = a_{\boldsymbol{k}}$. The interlayer DDI then introduces a coupling between $a_{\boldsymbol{k}}$ and $b_{\boldsymbol{k}}$ and generates hybrid eigenstates generally in the form of

$$\psi_{\boldsymbol{k}} = \frac{1}{\sqrt{2}} (a_{\boldsymbol{k}} + e^{i\delta_{\boldsymbol{k}}} b_{\boldsymbol{k}}). \quad (71)$$

The phase factor $\delta_{\boldsymbol{k}}$ relies on the explicit expression of the coupling. The $\mathcal{PT}$ partner of $\psi_{\boldsymbol{k}}$ reads

$$\mathcal{PT} \psi_{\boldsymbol{k}} = e^{-i\delta_{\boldsymbol{k}}} \frac{1}{\sqrt{2}} (a_{\boldsymbol{k}} + e^{i\delta_{\boldsymbol{k}}} b_{\boldsymbol{k}}), \quad (72)$$

equivalent to ψ_k except a marginal global phase factor $e^{-i\delta_k}$. In other words, ψ_k itself is $\mathcal{PT}$ symmetric and no additional degeneracy is necessary. By contrast, the relation $(\mathcal{PT})^2 = -1$ in fermionic systems results in the $\mathcal{PT}$ partner of a hybrid state Eq. (71) as

$$\mathcal{PT}\psi_k = e^{-i\delta_k}\frac{1}{\sqrt{2}}(-a_k + e^{i\delta_k}b_k), \tag{73}$$

which is orthogonal to ψ_k, indicating that $\mathcal{PT}\psi_k$ and ψ_k must be different states.

IV. SUMMARY

In summary, we predict magnon spin-orbit coupling due to DDI in monoclinic-stacked van der Waals antiferromagnetic bilayers. Such a spin-orbit coupling is expected to activate the intrinsic magnon spin-relaxation mechanism and magnon spin Hall effect recently predicted in Ref. [13]. Specifically, in the long wavelength limit, the spin-orbit coupling contains both momentum-independent and linearly momentum-dependent effective magnetic fields, which give rise to two nodal points. Due to their low energy, these magnon states would have a large thermal population and are relevant even at low temperature. The sub-THz range of their frequencies, although much higher than the usual ferromagnetic resonance, is already achievable by current techniques [10,11,14,15], which supports their observation and potential applications in magnonics. In the K and K' valleys, four nodal points are found in each valley. These nodal points connect the acoustic and optical magnon bands and make a magnonic semimetal. By tuning the interlayer distance or introducing intralayer Kitaev interaction, a phase transition to insulating phase is predicted.

APPENDIX A: DIPOLAR INTERACTION IN THE LONG WAVELENGTH LIMIT

We now calculate the summation appearing in the interlayer DDI:

$$F_k^{\alpha\beta} = -3\sum_{mn}\frac{(X_{mn}^{\alpha\beta} - iY_{mn}^{\alpha\beta})^2}{(R_{mn}^{\alpha\beta})^5}e^{ik\cdot R_{mn}^{\alpha\beta}}. \tag{A1}$$

Focusing on the long wavelength regime, one can take a cutoff distance ρ satisfying $1/k \gg \rho \gg a_0$. For all in-plane distances shorter than ρ, it is safe to use $e^{ik\cdot R_{mn}^{\alpha\beta}} \simeq 1$,

$$F^{\alpha\beta}(k) \simeq -3\sum_{|k\cdot R_{mn}^{\alpha\beta}|>k\rho}\frac{(X_{mn}^{\alpha\beta} - iY_{mn}^{\alpha\beta})^2}{(R_{mn}^{\alpha\beta})^5}e^{ik\cdot R_{mn}^{\alpha\beta}}$$

$$-3\sum_{|k\cdot R_{mn}^{\alpha\beta}|<k\rho}\frac{(X_{mn}^{\alpha\beta} - iY_{mn}^{\alpha\beta})^2}{(R_{mn}^{\alpha\beta})^5}$$

$$= -\frac{1}{A}\int_{r>\rho}dre^{ik\cdot r}(\partial_x^2 - \partial_y^2 - 2i\partial_x\partial_y)\frac{1}{\sqrt{r^2+h^2}}$$

$$-\frac{1}{A}(\beta_{xx}^{\alpha\beta} - \beta_{yy}^{\alpha\beta} - 2i\beta_{xy}^{\alpha\beta}), \tag{A2}$$

with A being the area of a unit cell and h the interlayer distance. Apparently, the atomistic detail of a specific crystal only affects the k-independent parameters $\beta_{ij}^{\alpha\beta}$. The k-dependent term can be calculated analytically.

By applying partition integration, one obtains

$$\int_{r>\rho}dxdye^{ik\cdot r}\partial_y^2\frac{1}{\sqrt{r^2+h^2}}$$

$$= -\left(\oint_L dxe^{ik\cdot r}\frac{y}{(r^2+h^2)^3} - \oint_{r=\rho}dxe^{ik\cdot r}\frac{y}{(r^2+h^2)^{3/2}}\right)$$

$$+ik_y\oint_L dxe^{ik\cdot r}\frac{1}{\sqrt{r^2+h^2}} - ik_y\oint_{r=\rho}dxe^{ik\cdot r}\frac{1}{\sqrt{r^2+h^2}}$$

$$-k_y^2\int_{r>\rho}dxdye^{ik\cdot r}\frac{1}{\sqrt{r^2+h^2}}. \tag{A3}$$

Here, L represents the outer boundary of the entire 2D system, which is assumed be to sufficiently large so the factor $e^{-ik\cdot r}$ oscillates at the boundary, resulting in a significant reduction of the integration over L. At the inner surface with $r = \rho$, we have $e^{-ik\cdot r} \simeq 1$. Considering the interlayer distance h of the same order of a_0, we have $h \ll \rho$ and therefore $\sqrt{r^2+h^2} \approx r$ for $r \geqslant \rho$. Equation (A3) then gives

$$\int_{r>\rho}dxdye^{ik\cdot r}\partial_y^2\frac{1}{\sqrt{r^2+h^2}}$$

$$\simeq \frac{2\pi\rho^2}{(\rho^2+h^2)^{3/2}} - \frac{k_y^2}{k}\int_0^{2\pi}d\theta\int_{k\rho}^\infty d\xi e^{i\xi\cos\theta}$$

$$= \frac{2\pi\rho^2}{(\rho^2+h^2)^{3/2}} - 2\pi\frac{k_y^2}{k}. \tag{A4}$$

Similarly, one can calculate the other two integrals in Eq. (A2):

$$\int_{r>\rho}dxdye^{ik\cdot r}\partial_x^2\frac{1}{\sqrt{r^2+h^2}} = \frac{2\pi\rho^2}{(\rho^2+h^2)^{3/2}} - 2\pi\frac{k_x^2}{k}, \tag{A5}$$

$$\int_{r>\rho}dxdye^{ik\cdot r}\partial_y\partial_x\frac{1}{\sqrt{r^2+h^2}} = -2\pi\frac{k_yk_y}{k}. \tag{A6}$$

Therefore, the summation Eq. (A1) can be expressed as

$$F_k^{\alpha\beta} = \frac{1}{A}(\beta_{yy}^{\alpha\beta} - \beta_{xx}^{\alpha\beta} + 2i\beta_{xy}^{\alpha\beta} + 2\pi ke^{-2i\theta_k}), \tag{A7}$$

with θ_k representing the angle of k with respect to the x axis.

The spin-orbit-coupling parameters of the acoustic and optical bands read

$$\zeta_k \pm \eta_{+,k} = \frac{S\mu_0(g\mu_B)^2}{2}\left(F_k^{d_1a_1} \mp \frac{F_k^{d_1a_2} + F_k^{d_2a_1}}{2}\right), \tag{A8}$$

which contain nine parameters $\beta_{ij}^{\alpha\beta}$. However, these parameters are actually not independent, because any vector $R^{d_2a_1}$ ($R^{d_1a_2}$) can be obtained by rotating one particular $R^{d_1a_1}$ around

the z axis counterclockwise by $2\pi/3$ ($-2\pi/3$). Specifically, we find

$$\boldsymbol{R}_{mn,\parallel}^{d_1 a_1} = a_0 \begin{pmatrix} \sqrt{3}m - \frac{\sqrt{3}}{2}n - \frac{2\sqrt{3}}{3} \\ \frac{3}{2}n \end{pmatrix}, \tag{A9}$$

$$\boldsymbol{R}_{(m-n)(-n),\parallel}^{d_2 a_1} = a_0 \begin{pmatrix} -\frac{\sqrt{3}}{2}m - \frac{\sqrt{3}}{2}n + \frac{\sqrt{3}}{3} \\ \frac{3}{2}m - \frac{3}{2}n - 1 \end{pmatrix}$$

$$= \mathcal{R}(2\pi/3)\boldsymbol{R}_{mn,\parallel}^{d_1 a_1}, \tag{A10}$$

$$\boldsymbol{R}_{(-n)(m-4n-2),\parallel}^{d_1 a_2} = a_0 \begin{pmatrix} -\frac{\sqrt{3}}{2}m + \sqrt{3}n + \frac{\sqrt{3}}{3} \\ -\frac{3}{2}m + 1 \end{pmatrix}$$

$$= \mathcal{R}(-2\pi/3)\boldsymbol{R}_{mn,\parallel}^{d_1 a_1}, \tag{A11}$$

where the rotation operator around normal direction is defined as

$$\mathcal{R}(\phi) = \begin{pmatrix} \cos\phi & -\sin\phi \\ \sin\phi & \cos\phi \end{pmatrix}. \tag{A12}$$

By writing the $\beta_{ij}^{\alpha\beta}$ in the form of matrices, we express them as

$$\hat{\beta}^{d_1 a_1} = \begin{pmatrix} \beta_{xx} & \beta_{xy} \\ \beta_{xy} & \beta_{yy} \end{pmatrix}, \tag{A13}$$

$$\hat{\beta}^{d_2 a_1} = \mathcal{R}(2\pi/3)\hat{\beta}(\zeta)\mathcal{R}(-2\pi/3), \tag{A14}$$

$$\hat{\beta}^{d_1 a_2} = \mathcal{R}(-2\pi/3)\hat{\beta}(\zeta)\mathcal{R}(2\pi/3), \tag{A15}$$

which give

$$F_{\boldsymbol{k}}^{d_1 a_1} = \beta_{yy} - \beta_{xx} + 2i\beta_{xy} + 2\pi k e^{-2i\theta_k}, \tag{A16}$$

$$F_{\boldsymbol{k}}^{d_2 a_1} = \left(\frac{1}{2} - \frac{i\sqrt{3}}{2}\right)(\beta_{xx} - \beta_{yy})$$

$$- 2\left(\frac{\sqrt{3}}{2} + \frac{i}{2}\right)\beta_{xy} + 2\pi k e^{-2i\theta_k}, \tag{A17}$$

$$F_{\boldsymbol{k}}^{d_1 a_2} = \left(\frac{1}{2} + \frac{i\sqrt{3}}{2}\right)(\beta_{xx} - \beta_{yy})$$

$$- 2\left(-\frac{\sqrt{3}}{2} + \frac{i}{2}\right)\beta_{xy} + 2\pi k e^{-2i\theta_k}. \tag{A18}$$

In addition, for any vector $\boldsymbol{R}_{mn}^{a_1 d_1} = (X_{mn}^{a_1 d_1}, Y_{mn}^{a_1 d_1}, Z_{mn}^{a_1 d_1}) = (\sqrt{3}m - \sqrt{3}n/2 - 2\sqrt{3}/3, 3n/2, 2\eta_z)a_0$ with nonzero n, one can always find another vector $\boldsymbol{R}_{(m-n)(-n)}^{a_1 d_1} = (\sqrt{3}m - \sqrt{3}n/2 - 2\sqrt{3}/3, -3n/2, 2\eta_z)a_0 = (X_{mn}^{a_1 d_1}, -Y_{mn}^{a_1 d_1}, Z_{mn}^{a_1 d_1})$. Their contributions to β_{xy} cancel with each other, meaning $\beta_{xy} \equiv 0$ in the present lattice.

Finally, we obtain

$$\zeta_{\boldsymbol{k}} \pm \eta_{+,\boldsymbol{k}} = \left(1 \pm \frac{1}{2}\right)\mu_0\mu_B M_s^{2D}(\beta_{yy} - \beta_{xx})$$

$$+ (1 \mp 1)\mu_0\mu_B M_s^{2D} 2\pi k e^{-2i\theta_k}, \tag{A19}$$

with $M_s^{2D} = Sg^2\mu_B/(2A)$. Thus, the spin-orbit coupling in the acoustic and optical bands become

$$\zeta_{\boldsymbol{k}} - \eta_{+,\boldsymbol{k}} = -f_0 + v_0 k e^{-2i\theta_k} \tag{A20}$$

and

$$\zeta_{\boldsymbol{k}} + \eta_{+,\boldsymbol{k}} = -3f_0, \tag{A21}$$

respectively. Here, $f_0 = \frac{1}{2}\mu_0\mu_B M_s^{2D}(\beta_{xx} - \beta_{yy})$ and $v_0 = \mu_0\mu_B 4\pi M_s^{2D}$. The value of f_0 can be determined from the numerical evaluation at $k = 0$ in a lattice model.

Similarly, for the intralayer parameters, we have

$$G_{\boldsymbol{k}}^{\alpha\beta} \simeq -\frac{1}{A}\beta_{zz}^{\alpha\beta} - \frac{1}{A}\int_{r>\rho} d\boldsymbol{r} e^{i\boldsymbol{k}\cdot\boldsymbol{r}}\partial_z^2 \frac{1}{\sqrt{r^2 + h^2}}. \tag{A22}$$

Using $\sqrt{r^2 + h^2} \approx r$ for $r \geqslant \rho$, the second term gives

$$\int_{r>\rho} dx\,dy\, e^{i\boldsymbol{k}\cdot\boldsymbol{r}}\partial_z^2 \frac{1}{\sqrt{r^2 + h^2}} \simeq k\int_0^{2\pi} d\theta \int_{k\rho}^{\infty} d\xi\, e^{i\xi\cos\theta}$$

$$= 2\pi k, \tag{A23}$$

leading to

$$\epsilon_{\boldsymbol{k}}' = A_{\boldsymbol{k}}^{a_1 a_1} = -\frac{S\mu_0(g\mu_B)^2}{2}G_{\boldsymbol{k}}^{a_1 a_1}$$

$$= \mu_0\mu_B M_s^{2D}\left(\beta_{zz}^{a_1 a_1} + 2\pi k\right) = f_z + \frac{1}{2}v_0 k, \tag{A24}$$

$$\lambda_{\boldsymbol{k}}' = A_{\boldsymbol{k}}^{a_1 a_2} = -\frac{S\mu_0(g\mu_B)^2}{2}G_{\boldsymbol{k}}^{a_1 a_2}$$

$$= \mu_0\mu_B M_s^{2D}\left(\beta_{zz}^{a_1 a_2} + 2\pi k\right) = f_z' + \frac{1}{2}v_0 k. \tag{A25}$$

APPENDIX B: RELATION BETWEEN THE SPIN-ORBIT COUPLING PARAMETERS AT K AND K' POINTS

According to the rotation relation addressed above, one expresses the vectors as

$$\boldsymbol{R}_{mn,\parallel}^{d_1 a_1} = \begin{pmatrix} R_{mn,\parallel}^{d_1 a_1}\cos\theta_{mn} \\ R_{mn,\parallel}^{d_1 a_1}\sin\theta_{mn} \end{pmatrix}, \tag{B1}$$

$$\boldsymbol{R}_{(m-n)(-n),\parallel}^{d_2 a_1} = \begin{pmatrix} R_{mn,\parallel}^{d_1 a_1}\cos\left(\theta_{mn} + \frac{2\pi}{3}\right) \\ R_{mn,\parallel}^{d_1 a_1}\sin\left(\theta_{mn} + \frac{2\pi}{3}\right) \end{pmatrix}, \tag{B2}$$

$$\boldsymbol{R}_{(-n)(m-4n-2),\parallel}^{d_1 a_2} = \begin{pmatrix} R_{mn,\parallel}^{d_1 a_1}\cos\left(\theta_{mn} - \frac{2\pi}{3}\right) \\ R_{mn,\parallel}^{d_1 a_1}\sin\left(\theta_{mn} - \frac{2\pi}{3}\right) \end{pmatrix}. \tag{B3}$$

By applying them into the general expression of spin-orbit-coupling parameters, we have

$$\zeta_{K(K')} = -\frac{3S\mu_0(g\mu_B)^2}{2}\sum_{mn}\frac{\left(R_{mn,\parallel}^{d_1 a_1}\right)^2}{\left(R_{mn}^{d_1 a_1}\right)^5}e^{-2i\theta_{mn}}$$

$$\times e^{i\boldsymbol{K}(\boldsymbol{K}')\cdot\boldsymbol{R}_{mn}^{d_1 a_1}} \tag{B4}$$

$$\eta_{K(K')}' = -\frac{3S\mu_0(g\mu_B)^2}{2}\sum_{mn}\frac{\left(R_{mn,\parallel}^{d_1 a_1}\right)^2}{\left(R_{mn}^{d_1 a_1}\right)^5}e^{-2i(\theta_{mn} - \frac{2\pi}{3})}$$

$$\times e^{i\boldsymbol{K}(\boldsymbol{K}')\cdot\boldsymbol{R}_{(-n)(m-4n-2)}^{d_1 a_2}} \tag{B5}$$

$$\eta_{K(K')} = -\frac{3S\mu_0(g\mu_B)^2}{2}\sum_{mn}\frac{\left(R_{mn,\parallel}^{d_1 a_1}\right)^2}{\left(R_{mn}^{d_1 a_1}\right)^5}e^{-2i(\theta_{mn} + \frac{2\pi}{3})}$$

$$\times e^{i\boldsymbol{K}(\boldsymbol{K}')\cdot\boldsymbol{R}_{(m-n)(-n)}^{d_2 a_1}} \tag{B6}$$

at K and K' points. By further substituting

$$\boldsymbol{K}(\boldsymbol{K}') = \left(\mp \frac{4\pi}{3\sqrt{3}a_0}, 0\right), \tag{B7}$$

we obtain the relations

$$\zeta_K = \eta'_K = \eta_K e^{-i4\pi/3}, \tag{B8}$$

$$\zeta_{K'} = \eta_{K'} = \eta'_{K'} e^{i4\pi/3}. \tag{B9}$$

Here, the upper and lower signs stand for the K and K', respectively.

For the parameter $\lambda'_{\mathbf{k}}$, the involved vectors satisfy C_3 rotation symmetry, i.e.,

$$\boldsymbol{R}^{a_1 a_2}_{mn,\parallel} = a_0 \begin{pmatrix} \sqrt{3}m + \frac{\sqrt{3}}{2}n \\ \frac{3}{2}n + 1 \end{pmatrix}, \tag{B10}$$

$$\boldsymbol{R}^{a_1 a_2}_{(-m-n)(m-1),\parallel} = \mathcal{R}(2\pi/3)\boldsymbol{R}^{a_1 a_2}_{mn,\parallel}, \tag{B11}$$

$$\boldsymbol{R}^{a_1 a_2}_{(n+1)(-m-n-1),\parallel} = \mathcal{R}(-2\pi/3)\boldsymbol{R}^{a_1 a_2}_{m,\parallel}. \tag{B12}$$

This allows us to transform the summation around K (K') into

$$\begin{aligned} \lambda'_{K(K')+\boldsymbol{q}} &= -\frac{S\mu_0(g\mu_B)^2}{2}\sum_{mn}\frac{(R^{a_1 a_2}_{mn}) - 3(Z^{a_1 a_2}_{mn})^2}{(R^{a_1 a_2}_{mn})^5} \\ &\quad \times e^{i(\mp\mathbf{K}_0+\boldsymbol{q})\cdot\boldsymbol{R}^{a_1 a_2}_{mn}}, \end{aligned} \tag{B13}$$

$$\begin{aligned} &= -\frac{S\mu_0(g\mu_B)^2}{2}\sum_{mn}\frac{(R^{a_1 a_2}_{mn}) - 3(Z^{a_1 a_2}_{mn})^2}{(R^{a_1 a_2}_{mn})^5} \\ &\quad \times \frac{1}{3}[e^{i(\mp\mathbf{K}_0+\boldsymbol{q})\cdot\boldsymbol{R}^{a_1 a_2}_{mn}} + e^{i(\mp\mathbf{K}_0+\boldsymbol{q})\cdot\boldsymbol{R}^{a_1 a_2}_{(-m-n)(m-1)}} \\ &\quad + e^{i(\mp\mathbf{K}_0+\boldsymbol{q})\cdot\boldsymbol{R}^{a_1 a_2}_{(n+1)(-m-n-1)}}]. \end{aligned} \tag{B14}$$

We then expand it up to the linear order in q. Actually the zeroth order vanishes. The linear order leads to

$$\lambda'_{K(K')+\boldsymbol{q}} = \pm e^{\pm i\theta_q} q v_m, \tag{B15}$$

with

$$\begin{aligned} v_m &= -\frac{S\mu_0(g\mu_B)^2}{4}\sum_{mn}\frac{(R^{a_1 a_2}_{mn}) - 3(Z^{a_1 a_2}_{mn})^2}{(R^{a_1 a_2}_{mn})^4} \\ &\quad \times \sin\left[\frac{4\pi}{3}(m-n) + \theta_{mn}\right]. \end{aligned} \tag{B16}$$

Equation (B15) has the same form as the exchange term,

$$\lambda_{K(K')+\boldsymbol{q}} = -\omega_{\text{ex}}\gamma_{K(K')+\boldsymbol{q}} = \mp v_F q e^{\pm i\theta_q}, \tag{B17}$$

where the exchange-induced velocity $v_F = a_0\omega_{\text{ex}}/2$. As a result, we obtain

$$\lambda_{K(K')+\boldsymbol{q}} + \lambda'_{K(K')+\boldsymbol{q}} = \mp(v_F - v_m)q e^{\pm i\theta_q}. \tag{B18}$$

Typically, the intralayer exchange interaction is much stronger than DDI, which leads to $v_F \gg v_m$ and

$$\begin{aligned} \eta_{\pm,K+\boldsymbol{q}} &= -(\eta'_K e^{-i\theta_q} \pm \eta_K e^{i\theta_q})/2 \\ &= -\zeta_K[e^{-i\theta_q} \pm e^{i(\theta_q - 2\pi/3)}]/2, \end{aligned} \tag{B19}$$

$$\begin{aligned} \eta_{\pm,K'+\boldsymbol{q}} &= (\eta'_{K'} e^{i\theta_q} \pm \eta_{K'} e^{-i\theta_q})/2 \\ &= \pm\zeta_{K'}[e^{-i\theta_q} \pm e^{i(\theta_q + 2\pi/3)}]/2. \end{aligned} \tag{B20}$$

By using Eqs. (B10)–(B12), one can also calculate the particle-hole coupling induced by intralayer DDI:

$$\begin{aligned} B^{a_1 a_2}_{K(K')} &= B^{a_2 a_1}_{K'(K)} \\ &= -\frac{3S\mu_0(g\mu_B)^2}{2}\sum_{mn}\frac{e^{-2i\theta_{mn}}}{(R^{a_1 a_2}_{mn})^3}e^{\mp i\mathbf{K}_0\cdot\boldsymbol{R}^{a_1 a_2}_{mn}} \\ &= -\frac{S\mu_0(g\mu_B)^2}{2}\sum_{mn}\frac{e^{-2i\theta_{mn}}}{(R^{a_1 a_2}_{mn})^3}e^{\mp i\mathbf{K}_0\cdot\boldsymbol{R}^{a_1 a_2}_{mn}} \\ &\quad + \frac{e^{-2i\theta_{(-m-n)(m-1)}}}{(R^{a_1 a_2}_{(-m-n)(m-1)})^3}e^{\mp i\mathbf{K}_0\cdot\boldsymbol{R}^{a_1 a_2}_{(-m-n)(m-1)}} \\ &\quad + \frac{e^{-2i\theta_{(n+1)(-m-n-1)}}}{(R^{a_1 a_2}_{(n+1)(-m-n-1)})^3}e^{\mp i\mathbf{K}_0\cdot\boldsymbol{R}^{a_1 a_2}_{(n+1)(-m-n-1)}} \\ &= f_K[1 + e^{i\frac{2\pi}{3}(1\pm 1)} + e^{-i\frac{2\pi}{3}(1\pm 1)}], \end{aligned} \tag{B21}$$

with

$$f_K = -\frac{S\mu_0(g\mu_B)^2}{2}\sum_{mn}\frac{e^{-2i\theta_{mn}}}{(R^{a_1 a_2}_{mn})^3}e^{\mp i\frac{4\pi}{3}(m-n)}. \tag{B22}$$

[1] C. Gong, L. Li, Z. Li, H. Ji, A. Stern, Y. Xia, T. Cao, W. Bao, C. Wang, Y. Wang *et al.*, Nature **546**, 265 (2017).

[2] B. Huang, G. Clark, E. Navarro-Moratalla, D. R. Klein, R. Cheng, K. L. Seyler, D. Zhong, E. Schmidgall, M. A. McGuire, D. H. Cobden *et al.*, Nature **546**, 270 (2017).

[3] N. D. Mermin and H. Wagner, Phys. Rev. Lett. **17**, 1133 (1966).

[4] N. Sivadas, S. Okamoto, X. Xu, C. J. Fennie, and D. Xiao, Nano Lett. **18**, 7658 (2018).

[5] P. Jiang, C. Wang, D. Chen, Z. Zhong, Z. Yuan, Z.-Y. Lu, and W. Ji, Phys. Rev. B **99**, 144401 (2019).

[6] Z. Sun, Y. Yi, T. Song, G. Clark, B. Huang, Y. Shan, S. Wu, D. Huang, C. Gao, Z. Chen *et al.*, Nature **572**, 497 (2019).

[7] H. Wang, C. Du, P. C. Hammel, and F. Yang, Phys. Rev. Lett. **113**, 097202 (2014).

[8] Z. Qiu, J. Li, D. Hou, E. Arenholz, A. T. N'Diaye, A. Tan, K. ichi Uchida, K. Sato, S. Okamoto, Y. Tserkovnyak *et al.*, Nat. Commun. **7**, 12670 (2016).

[9] R. Lebrun, A. Ross, S. A. Bender, A. Qaiumzadeh, L. Baldrati, J. Cramer, A. Brataas, R. A. Duine, and M. Klaui, Nature **561**, 222 (2018).

[10] J. Li, C. B. Wilson, R. Cheng, M. Lohmann, M. Kavand, W. Yuan, M. Aldosary, N. Agladze, P. Wei, M. S. Sherwin *et al.*, Nature **578**, 70 (2020).

[11] P. Vaidya, S. A. Morley, J. van Tol, Y. Liu, R. Cheng, A. Brataas, D. Lederman, and E. del Barco, Science **368**, 160 (2020).

[12] J. Lan, W. Yu, and J. Xiao, Nat. Commun. **8**, 178 (2017).

[13] K. Shen, Phys. Rev. Lett. **124**, 077201 (2020).

[14] X.-X. Zhang, L. Li, D. Weber, J. Goldberger, K. F. Mak, and J. Shan, Nat. Mater. **19**, 838 (2020).

[15] J. Cenker, B. Huang, N. Suri, P. Thijssen, A. Miller, T. Song, T. Taniguchi, K. Watanabe, M. A. McGuire, D. Xiao *et al.*, Nat. Phys. (2020), doi: 10.1038/s41567-020-0999-1.

[16] T. Holstein and H. Primakoff, Phys. Rev. **58**, 1098 (1940).

[17] K. Shen, Phys. Rev. B **100**, 094423 (2019).

[18] L. Chen, J.-H. Chung, B. Gao, T. Chen, M. B. Stone, A. I. Kolesnikov, Q. Huang, and P. Dai, Phys. Rev. X **8**, 041028 (2018).

[19] J.-Y. You, C. Chen, Z. Zhang, X.-L. Sheng, S. A. Yang, and G. Su, Phys. Rev. B **100**, 064408 (2019).

[20] J. Liu, L. Wang, and K. Shen, Phys. Rev. Research **2**, 023282 (2020).

[21] X. Wan, A. M. Turner, A. Vishwanath, and S. Y. Savrasov, Phys. Rev. B **83**, 205101 (2011).

[22] A. A. Burkov and L. Balents, Phys. Rev. Lett. **107**, 127205 (2011).

[23] S.-Y. Xu, I. Belopolski, N. Alidoust, M. Neupane, G. Bian, C. Zhang, R. Sankar, G. Chang, Z. Yuan, C.-C. Lee *et al.*, Science **349**, 613 (2015).

[24] B. Q. Lv, H. M. Weng, B. B. Fu, X. P. Wang, H. Miao, J. Ma, P. Richard, X. C. Huang, L. X. Zhao, G. F. Chen *et al.*, Phys. Rev. X **5**, 031013 (2015).

[25] E. Aguilera, R. Jaeschke-Ubiergo, N. Vidal-Silva, L. E. F. Foa Torres, and A. S. Nunez, Phys. Rev. B **102**, 024409 (2020).

[26] A. Kitaev, Ann. Phys. **321**, 2 (2006).

[27] C. Xu, J. Feng, H. Xiang, and L. Bellaiche, npj Comput. Mater. **4**, 57 (2018).

[28] P. Tang, Q. Zhou, G. Xu, and S.-C. Zhang, Nat. Phys. **12**, 1100 (2016).